

# Bidirectional Microrocker Bots with Sharp Tips Actuated by a Single Electromagnet

DeaGyu Kim<sup>a,1,2</sup>, Tony Wang<sup>a,3</sup>, Yifan Shi<sup>a</sup>, Zhijian Hao<sup>a</sup>, and Azadeh Ansari<sup>a</sup>

<sup>a</sup>School of Electrical and Computer Engineering, Georgia Institute of Technology, Atlanta, Georgia, USA

This manuscript was compiled on October 21, 2020

The recent advancements in nanoscale 3D printing and microfabrication techniques have reinvigorated research on microrobotics and nanomachines. However, precise control of the robot motion and navigation on biological environments have remained challenging to date. This work presents the first demonstration of magnetic microscale rocker robot (microrocker bot) capable of bidirectional movement on flat as well as biological surfaces, when actuated by a single compact electromagnet. The  $100\mu\text{m} \times 113\mu\text{m} \times 36\mu\text{m}$  robot was 3D printed via two-photon lithography and subsequently coated with a nickel (Ni) thin film. When actuated by an externally applied magnetic sawtooth field, the robot demonstrated stick-slip motion enabled by its rockers. The controllable bidirectional motion is enabled by adjusting the DC offset of the waveform, which tilts the robot and biases it towards either forward or backward motion. The microrocker bots are further equipped with sharp tips that can get engaged via application of DC-only magnetic fields. This novel control method offers an attractive solution to replace the multiple bulky coils traditionally used for magnetic actuation and control, as well as allows for a more flexible and simple approach towards microrobotics motion control. When the frequency and offset of the sawtooth waveform are optimized, the robot travels up to  $100\mu\text{m/s}$  (1 body length per second) forward and backward with minor deviance from linear trajectories. Finally, to prove the robot's capabilities in direct contact with biological environments, we demonstrate the microrobot's ability to traverse forward and backward on the surface of a *Dracaena Fragrans* (corn plant), as well as upend on its mechanical tip.

Microrobot | Magnetic Actuation | Steering | 3D Print | Mechanical Tip

Steerable untethered microscale robots with precise motion control and mechanical functionality offer significant advantages in micromanipulation (1–3), sample biopsy (4, 5), drug delivery (6–10), and microsurgery (11, 12) particularly by harnessing actuation power from external sources, as on-board actuators become infeasible at such extreme scales. The most common methods include acoustic/ultrasound (13–16), optical (17–20), electric (21, 22), and magnetic actuation (23–25). Optically-driven microrobots rely on an external laser induced heating to deform or generate fluid flow, leading to net propulsion in liquids. However, the light intensity is too strong for safe in-vivo operations (22) and may be attenuated or absorbed by the surrounding environment before reaching the robot. Microrobots moving via electrostatic forces require a specialized electric grid underneath or an electric field gradient, which suffers from a lack of biocompatibility (21). Ultrasound and magnetic actuation mechanisms are two of the most commonly used for biomedical applications due to their deep tissue penetration and strong propulsive forces (11, 26). Microrobots powered via ultrasound actuation rely on excitation at resonant frequency to achieve walking or mi-

crosswimming. In contrast, magnetic microrobots are guided by an external magnetic field waveform and undergo motion such as stick-slip (27), rotation (28), and metachronal wave deflection (29) for net displacement.

However, most magnetically driven microrobots rely on utilizing a multi-axis, often bulky, electromagnet system for controllable steering by generating rotating magnetic field (10, 24, 26, 30–45). Such multi-coil systems limit the working space to centimeter scales, limited by the confines of the electromagnets. This severely limits the in-vitro magnetic manipulation applications. Thus, a simpler setup with a compact electromagnet and yet capable of microrobot steering is desirable, allowing for a wider range of applications.

This paper presents a  $100\mu\text{m} \times 113\mu\text{m} \times 36\mu\text{m}$  magnetically actuated microscale rocker robot (microrocker bot) (Fig. 1A) capable of bidirectional movement across nonuniform biological surfaces using similar setup from (46). The microrocker bot uses rockers as shown in 1 to enable smoother motion, and to move either forward or backward, it relies on adjusting the DC offset of the magnetic field waveform to tilt the robot towards either forward or backward. This response was magnetically encoded into the robot's Ni thin film coating (Fig. 1B) due to its significantly higher remanence at nanoscale (47). The periodic oscillations in the magnetic field then allow for stick-slip motion and induces net displacement in each oscillation cycle. (Fig. 1C, Movie S1).

These robots displayed excellent linear trajectories in both

## Significance Statement

Microrobots show increasing potential as tools for interaction with and manipulation of microscale organisms, while maneuvering in otherwise inaccessible locations. Here, we present for the first time, a microrobot capable of controllable linear forward and backward motion on flat environments, as well as in direct contact with biological surfaces, by only changing the DC offset of the magnetic field from a single electromagnet. The microrobots use specially designed rockers instead of legs to navigate on non-flat environments. We present three microrocker bots walking in sync using stick-slip motion, with clear resonance-like dependence of their speed on the stepout frequency. Furthermore, the microrocker bots are equipped with sharp tips on the robot front, and can be engaged by applying a DC magnetic field.

D.K. and T.W. prepared samples and performed research. Y.S. and Z.H. processed data and provided figures. D.K., T.W., and A.A. analyzed the data and wrote the paper, and A.A. supervised research

The authors declare no competing interests.

<sup>1</sup>D.K. contributed equally to this work with T.W.

<sup>2</sup>Azadeh Ansari E-mail: azadeh.ansari@ece.gatech.edu

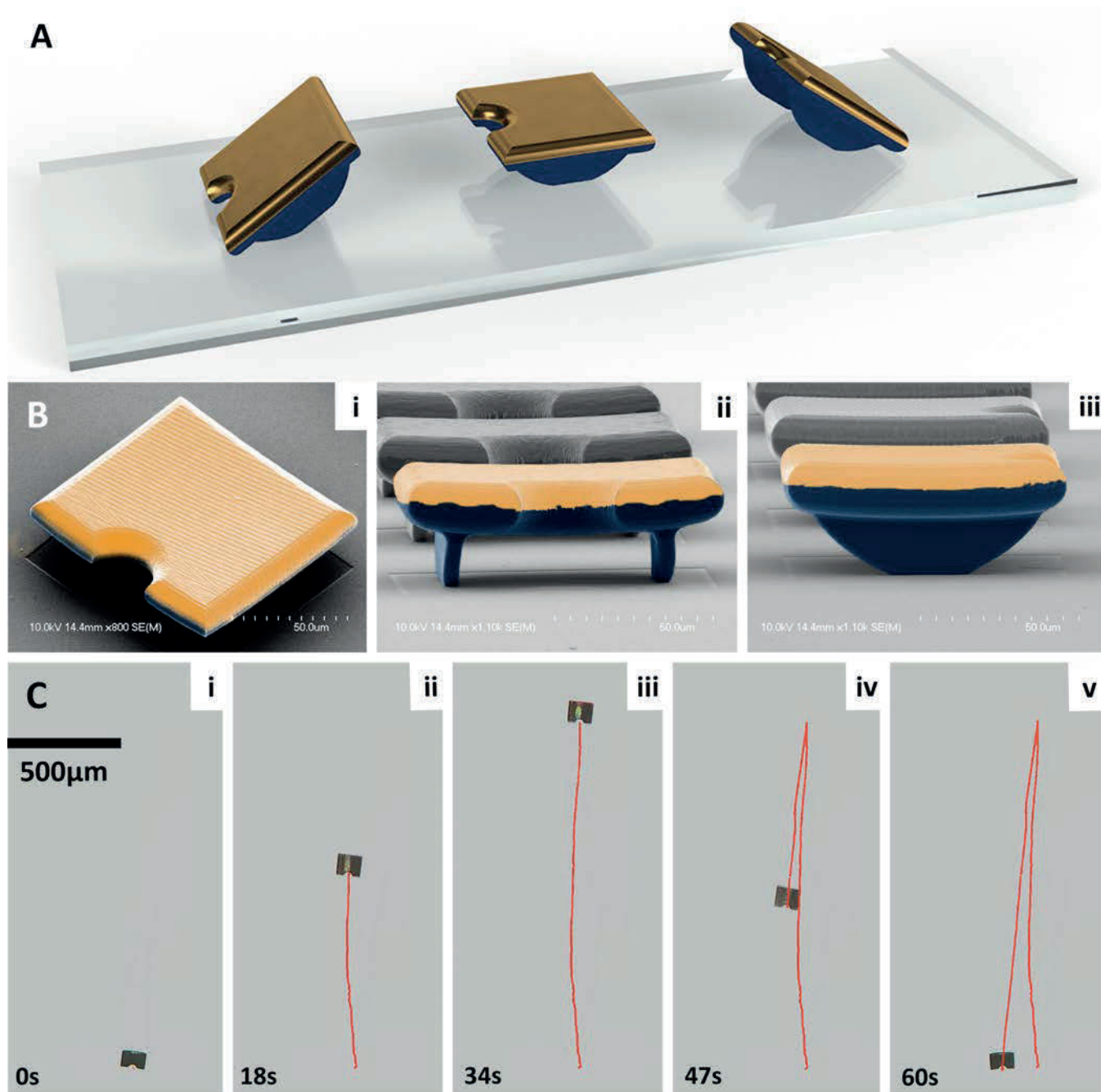


**Fig. 1.** (A) Schematic of the microrocker bot under (left) backward bias tilt, (middle) no bias or flat, and (right) forward bias tilt. The angles have been exaggerated in the drawings to highlight the importance of tilt bias in achieving bidirectionality. (B) False colored SEM images of the microrocker bots from a (i) isometric view, (ii) back view, and (iii) side view. The top Ni layer is shown with a gold color and the polymer is presented with navy. (C) Linear trajectory of the microrocker bot under a 2.82mT<sub>pp</sub> peak-to-peak magnetic sawtooth wave at 10Hz. The robot moves forward under a 307μT offset and backward under a -77μT offset (Movie S1).

directions and can walk on rougher and textured substrates, namely the surface of the common house plant *Dracaena Fragrans* (corn plant) leaf (Movie S4). And most importantly, the dependency of speed on stepout frequency of the robot shows similar response to resonance effect shown in (13) which can be the basis for transition into full 2D motion with single electromagnet system.

## Results

**Microrocker Bot Design.** The microrocker bot consists of an Ip-S (48) polymer body deposited with a 300nm Ni layer (Figure 1A). All robots were fabricated via two-photon lithography. A flat area to the rocker bottom was added to establish a stable contact and prevent the robot from falling off the substrate during fabrication. The robots were subsequently coated with 300nm Ni thin films via electron beam deposition. Due to the thermal contraction of Ni layer, compressive stress

was induced in the Ni layer and resulted in a slight upwards curvature (Figure 1B). The robots were then released from substrate by a probe manipulator.

**Robot Actuation and Bilinearity Principles.** When magnetized by a field  $\mathbf{H}$ , the Ni layer will retain some magnetic strength  $\mathbf{M} = \chi|\mathbf{H}|$ , where  $\chi$  is its magnetic susceptibility tensor (49). Furthermore, the geometry of Ni layer influences the susceptibility. When approximated as a prolate ellipsoid and aligned with the robot's principal axes to a chosen coordinate frame,  $\chi$  can be approximated by equation 1,

$$\chi = \text{diag}\left(\frac{X}{1 + N_a X}, \frac{X}{1 + N_r X}, \frac{X}{1 + N_r X}\right), \quad [1]$$

where  $X$  is the material magnetic susceptibility, and  $N_a$  and  $N_r$  are the demagnetization factors of the major and minor elliptical axes respectively. These demagnetization factors can be found from the equations 2, 3, and 4 (49).

$$N_a + 2N_r = 1 \quad [2]$$

$$N_a = \frac{1}{A^2 - 1} \left( \frac{A}{2\sqrt{A^2 - 1}} \ln \frac{A + \sqrt{A^2 - 1}}{A - \sqrt{A^2 - 1}} \right) \quad [3]$$

$$N_r = \frac{A^2}{A^2 - 1} \left( 1 - \frac{1}{\sqrt{A^2 - 1}} \sin^{-1} \frac{\sqrt{A^2 - 1}}{A} \right) \quad [4]$$

From the above equations, the demagnetization factor scales inversely with the aspect ratio  $A$ . This signifies that a flat deposited Ni layer with the thickness much smaller than the length and width would have a higher demagnetization factor along its height. As a result, the Ni thin film deposited on the robots will have a fixed magnetic polarization parallel rather than perpendicular to its planar surface (50).

Under a magnetic field, the Ni layer on the micro robot will align with the vertical magnetic field lines, inducing a torque, expressed as  $\mathbf{T} = V_m(\mathbf{M} \times \mathbf{B})$ , where  $V_m$  is the volume of the Ni layer,  $\mathbf{T}$  is the torque,  $\mathbf{M}$  is the Ni layer's magnetization, and  $\mathbf{B}$  is the applied magnetic field. In order to move, the robot must overcome its gravitational rest torque (34) expressed as:

$$T_g = \frac{\rho_g L V_m}{2} \quad [5]$$

where  $T_g$  is the rest torque and  $g$  is the gravitational acceleration. Here,  $\rho_e$  is the effective density of the robot when placed in a fluid with density  $\rho_f$  ( $\rho_e = \rho - \rho_f$ ).

In our experiments, we chose water as the fluid due to its relatively high density ( $\rho_f$ ) as well as minimization of the adhesive forces to the substrate. Furthermore, the robot's normal force,  $N$  is decreased due to buoyant force,  $F_B$ , and the gravitational rest torque is consequently reduced (equation 5). Figure 2A illustrates the experimental setup, with the microrocker bot fully submerged in water on top of an electromagnet that has a diameter of 8cm and is connected to a function generator.

Stick-slip motion in the rockers is achieved by applying an oscillating sawtooth voltage signal from the function generator connected to an electromagnet. The most common waveforms employed for magnetic actuation are square and sawtooth waves since they both have sudden changes in amplitude, which optimize the angular rotation during the slip phase.

Sawtooth waveform was chosen over square waveform due to its time asymmetry and better directionality (34).

A DC offset can additionally be introduced into the waveform to move the neutral angular position to be either forward tilt, backward tilt, or flat. As shown in (Fig. 2B), the DC offset plays a crucial role in the robot's resting position and the resulting direction of motion. For both forward and backward motion, the robots will experience the same torque direction for both the stick and slip phases. However, the DC offset during slow ramp will increase the robot's forward orientation ( $\uparrow \theta_1$ ) in forward bias, while decreasing its backward orientation ( $\downarrow \phi_1$ ). In steep decay, the reverse torque direction is applied, restoring the robot's initial orientations for both forward ( $\downarrow \theta_1$ ) and backward motion ( $\uparrow \phi_1$ ). These opposite changes in angle consequently lead to opposite directional movement simply by changing the offset voltage signal applied to a single electromagnet. In (34), the robot is kept in an inclined position via a secondary electromagnet while varying magnetic fields are applied by a primary electromagnet to induce a similar type of motion. In contrast, the microrocker bot presented in this work is actuated using a single electromagnet by optimizing the DC offset of the applied magnetic field signal.

The free body diagram of the microrocker bot is shown in Figure 2C. The magnetic forces applied on the robot are categorized into  $F_x$  and  $F_y$ , and the magnetic torque applied is  $T$ . The corresponding drag forces are labeled as  $D_x$ ,  $D_y$ , and  $D_T$ . The point of contact and center of mass are given by coordinates  $(P_x, P_y)$  and  $(x, y)$  respectively with  $r$  being distance between the two. Friction force, adhesion force, and buoyant force are labeled  $F_f$ ,  $F_a$ , and  $F_B$  respectively.  $\theta_o$  is the angle between flat of the rocker and  $r$ , and  $\theta$  is the changing angle relative to the surface. Based on these definitions, the equations of motion for the microrocker bot are given by equations 6, 7, and 8.

$$m\ddot{x} = F_x - F_f - D_x \quad [6]$$

$$m\ddot{y} = F_y - mg + N - D_y + F_B \quad [7]$$

$$J\ddot{\theta} = T + F_f r \sin(\theta + \theta_o) - (N - F_a) r \cos(\theta + \theta_o) - D_T \quad [8]$$

Assuming that the robot stays in contact with ground at all time, the critical point at which stick-slip transition occurs is given by equation 9,

$$\mu_s < \frac{\cos(\theta + \theta_o)}{\sin(\theta + \theta_o)} + \frac{(J\ddot{\theta} - T + D_T)}{Nr \sin(\theta + \theta_o)}, \quad [9]$$

where  $\mu_s$  is the static friction coefficient. The slip phase is determined by the angular position of the robot, the torque applied, and the angular acceleration of the robot. As the angular position of robot,  $\theta$ , decreases,  $\cos(\theta + \theta_o)$  increases and  $\sin(\theta + \theta_o)$  decreases, which increases the first half of equation 9. However, if the torque applied is in the positive direction, the second half of equation 9 also increases which works against transitioning into the slip regime. In the opposite scenario, if a large torque is applied in negative direction, it aids in transitioning into the slip regime. In forward motion, the decrease in  $\theta$  and large negative torque applied results in transition to slip regime. In backward motion, steep decay of sawtooth function results in large  $J\ddot{\theta}$ , which dominates and causes the transition into slip regime.



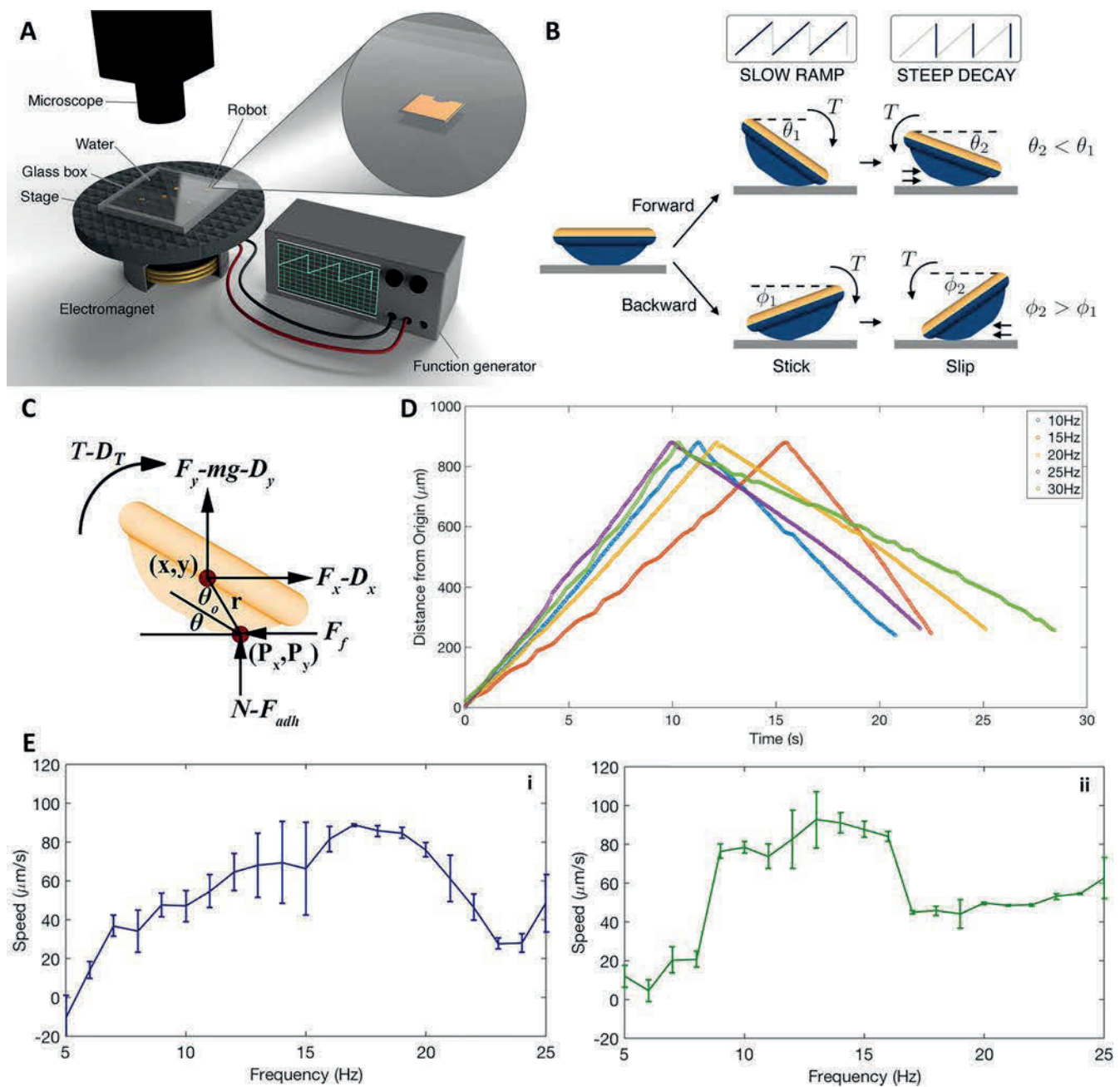


**Fig. 2.** (A) Experimental setup for microrocker bot actuation, imaging and characterization. (B) Schematic of forward and backward motions with the magnetic sawtooth waveform. Slow ramp and steep decay correspond to the rate of change in magnetic field of the sawtooth waveform. (C) Free body diagram of the microrocker bot under magnetic torque along with the relevant forces. (D) Trajectory of microrocker bot under various excitation frequencies of 10Hz, 15Hz, 20Hz, 25Hz, and 30Hz. Positive/negative slopes correspond to the robot forward/backward motions. (E) (i) Forward and (ii) backward frequency vs. speed response. Error bars represent 1 standard deviation in either direction from 3 repeated trials.

**Robot Speed.** Figure 2D shows the linear trajectories taken by a microrocker bot at various frequencies, where the lines with positive and negative slopes correspond to the forward and backward motions, respectively. For each frequency, the robot traversed  $900\mu\text{m}$  forward and  $700\mu\text{m}$  backward with a total distance of  $1.6\text{mm}$  travelled. Comparisons of the time taken to cover this distance between different conditions demonstrate that the speed of the robot depends on the actuation frequency. Furthermore, the strong linearity of the distance with time allows for rigorous linear regression to derive the robot speed.

Additionally, the linearity suggests that any inhomogeneity in the magnetic field gradient holds negligible influence over the trajectory. The minor deviation in the travelled distance linearity vs. time in 1C could be attributed to manufacturing nonidealities, resulting in the slight asymmetry of the rollers shown in Figure 1B(ii) or surface unevenness.

Figure 2E plots the frequency-speed response of the microrocker bot from 5Hz to 30Hz in 1Hz frequency increments. For all tests, the peak-to-peak amplitude of the magnetic field was  $2.82\text{mT}_{pp}$ , with  $307\mu\text{T}$  and  $-77\mu\text{T}$  DC offsets for forward

and backward motions, respectively. Additionally, 2E shows clear increase in speed and decrease in speed with relation to frequency with the critical frequency being known as stepout frequency. The difference between the stepout frequency of forward motion and backward motion is attributed to larger magnitude of DC offset of sawtooth magnetic field as the average rms value of the magnetic field applied increases, which results in increase of stepout frequency as shown by equation 10 (35),

$$\omega_s = \mu_0 ||m|| ||h|| / c, \quad [10]$$

where  $||h||$  is applied field magnitude,  $||m||$  is magnetic dipole moment of robot, and  $c$  is viscous drag coefficient. As a result, similar to the vibration powered microrobots, the magnetic microrobots show "resonance" behavior, associated with the frequency applied. From the experiments performed, the maximum speeds observed were  $100\mu\text{m/s}$  at 29Hz and  $108\mu\text{m/s}$  at 13Hz for forward and backward respectively.

**Robot Motion on a Leaf.** The microrobot was redesigned with a tip on its frontside to probe the leaf surface when vertically aligned with a DC magnetic field (Fig. 3A) as a proof of concept of controlled motion, with added probing functionality when in direct contact with a biological environment. The *Dracaena Fragrans* leaf along with a magnified image of a microrobot is shown on Figure 3C. As shown in Movie S4, the micro rocker bot exhibits linear forward and backward motion with average speeds of  $101\mu\text{m/s}$  and  $80\mu\text{m/s}$  respectively at 17Hz for forwards and backwards directions despite the comparatively rougher surface of the leaf.

Combined with strong linearity and precision, these results show promising applications for microsampling on biological surfaces. Future experiments will explore the microtip rocker bot's potential for cellular-level mechanical stimulation.

## Discussion

The demonstrated bidirectional and linear motions of the microrobot signify that a single coil setup is enough for precise bidirectional control. The demonstrated frequency dependence of speed of micro rocker bot show that the robot can be tuned to respond to specific stepout frequency by changing the material and thickness of film deposited, step-out frequency can be altered (35) which will lead to different frequency range required for actuation. This step-out frequency can be used for full 2D controlled movement. By using selective deposition via 3D printed deposition masks to introduce asymmetry in deposited film, different motions can be induced on the robot by altering both frequency and magnitude of the applied magnetic field waveform. Future experiments will thus focus on 2D movement of microrobot bots.

Further experiments with the microrobot bots have shown their capability to move in groups (Movie S5), demonstrating potential use for robotic swarm applications. This complex control could all be accomplished with a single, inexpensive, and compact electromagnet.

## Materials and Methods

**Microrobot Fabrication.** The microrobots were printed out of I-S photoresist on ITO (indium tin oxide) layered glass slide with a  $25\times$  objective using Nanoscribe Photonic Professional

GT, a two-photon-lithography tool (51). The robots were then developed in SU8 solution for 20 minutes and washed in IPA for 2 minutes. The mechanical properties of Ip-S, the material of the robot, are shown in Table 1. Robots' top surface were

**Table 1. Material properties of Ip-S polymer from Nanoscribe GmbH (48).**

Property	Value
Young's Modulus	4.6 GPa
Hardness	160 MPa
Storage Modulus	5 GPa
Loss Modulus	150-350 MPa
Shrinkage	2-12%
Density (liquid)	1.111 g/cm <sup>3</sup>

then deposited with 300nm nickel layer through electron beam deposition. The robots were released from the ITO-glass substrate using a probe manipulator. For experiments on the leaf surface, the robot was placed on its back and secured to the probe manipulator through adhesion contact force. It was then transferred to the leaf sample submerged in water.

**Experimental Setup.** The glass slide containing the robots was placed on top of a silicon substrate for better contrast in video. A square rim was then resin bonded to the slide. Afterwards, the rim was filled with water to minimize adhesive force and reduce normal force between the surface and robot. The slide was then placed on top of an electromagnet at its center. An Agilent 33220A function generator was connected to the electromagnet to supply the required waveform.

**Video and Image Processing.** A Moticam 1080 camera was connected to a top-down microscope (MPI TS150-THZ) to record the robots. Videos were analyzed using the DLTdv digitizing tool (52).

## Acknowledgment

This work was supported by Georgia Tech Institute for Electronics and Nanotechnology (IEN). The device fabrication was performed at the Georgia Tech Institute for Electronics and Nanotechnology clean room facilities, a member of the National Nanotechnology Coordinated Infrastructure (NNCI), which is supported by the National Science Foundation (Grant ECCS-1542174). The authors acknowledge Prof. Lily Cheung for the helpful discussions.

## 1. References

1. T Leong, et al., Tetherless thermobiochemically actuated microgrippers. *Proc. Natl. Acad. Sci.* **106**, 703–708 (2009).
2. E Steager, et al., Automated biomanipulation of single cells using magnetic microrobots. *The Int. J. Robotics Res.* **32**, 346–359 (2013).
3. S Tasoglu, E Diller, S Guven, M Sitti, U Demirci, Untethered micro-robotic coding of three-dimensional material composition. *Nat. Commun.* **5** (2014).
4. O Ergeneman, et al., A magnetically controlled wireless optical oxygen sensor for intraocular measurements. *IEEE Sensors J.* **8**, 29–37 (2008).
5. S Yim, E Gultepe, DH Gracias, M Sitti, Biopsy using a magnetic capsule endoscope carrying, releasing, and retrieving untethered microgrippers. *IEEE Transactions on Biomed. Eng.* **61**, 513–521 (2014).
6. S Lee, et al., A needle-type microrobot for targeted drug delivery by affixing to a microtissue. *Adv. Healthc. Mater.*, 1901697 (2020).
7. S Yim, K Goyal, M Sitti, (2013).
8. S Jeon, et al., Magnetically actuated microrobots as a platform for stem cell transplantation. *Sci. Robotics* **4** (2019).



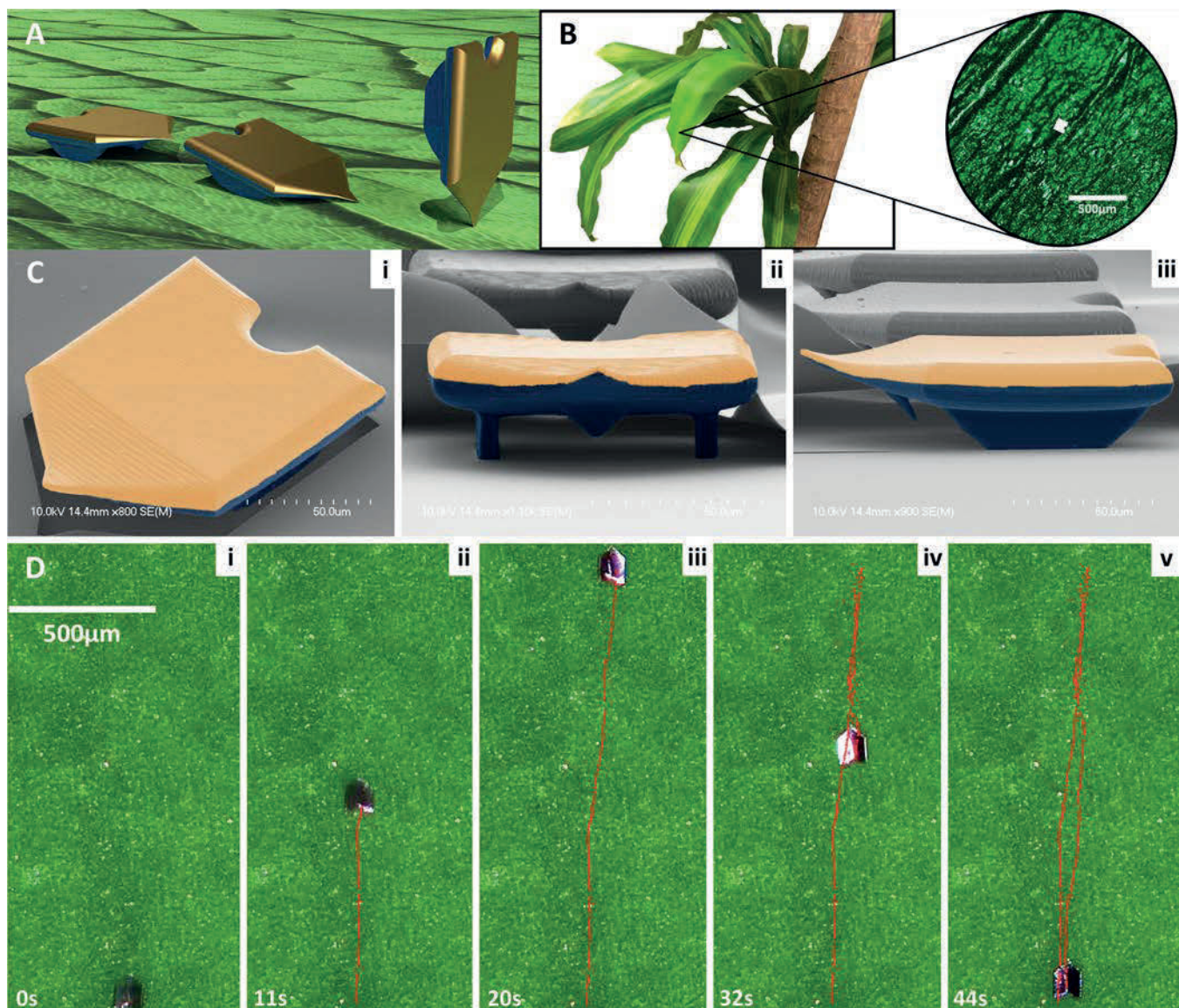


**Fig. 3.** (A) Schematic of micro-tip rocker bot under different magnetic field offsets. The robot at the far right completely aligns with the magnetic field. As a result, the tip contacts the leaf surface (B) *Dracaena Fragrans* plant with magnified image of microrocker bot on the leaf. (C) False colored SEM photos of the micro-tip rocker bot from a (i) isometric view, (ii) front view, and (iii) side view. A slight upwards bend is observable due to thermal stress. Gold = nickel, and navy = polymer. (D) Trajectory of the microtip rocker bot across the leaf surface at 10Hz.

9. S Lee, et al., Targeted drug and cell delivery: A capsule-type microrobot with pick-and-drop motion for targeted drug and cell delivery. *Adv. Healthc. Mater.* **7**, 1870036 (2018).
10. K Sangwon, et al., Magnetic microrobots: Fabrication and characterization of magnetic microrobots for three-dimensional cell culture and targeted transportation (adv. mater. 41/2013). *Adv. materials (Deerfield Beach, Fla.)* **25**, 5829 (2013).
11. M Sitti, et al., Biomedical applications of untethered mobile milli/microrobots. *Proc. IEEE* **103**, 205–224 (2015).
12. B Kratochvil, et al., Octomag: An electromagnetic system for 5-dof wireless micromanipulation. *2010 IEEE Int. Conf. on Robotics Autom.* (2010).
13. D Kim, Z Hao, J Ueda, A Ansari, A 5 mg micro-bristle-bot fabricated by two-photon lithography. *J. Micromechanics Microengineering* **29**, 105006 (2019).
14. D Ahmed, et al., Selectively manipulable acoustic-powered microswimmers. *Sci. Reports* **5** (2015).
15. YOWPSM Aghakhani, A., Acoustically powered surface-slipping mobile microrobots. *Proc. Natl. Acad. Sci.* **117**, 3469–3477 (2020).
16. D Ahmed, et al., Artificial swimmers propelled by acoustically activated flagella. *ACS Nano Lett.* **16** (2016).
17. W Hu, K Ishii, A Ohta, Micro-assembly using optically controlled bubble microrobots in saline solution. *2012 IEEE Int. Conf. on Robotics Autom.* (2012).
18. A Búzás, et al., Light sailboats: Laser driven autonomous microrobots. *Appl. Phys. Lett.* **101**, 041111 (2012).
19. O Sul, M Falvo, R Taylor, S Washburn, R Superfine, Thermally actuated untethered impact-driven locomotive microdevices. *Appl. Phys. Lett.* **89**, 203512 (2006).
20. MZ Miskin, et al., Electronically integrated, mass-manufactured, microscopic robots. *Nature* **584**, 557–561 (2020).
21. B Donald, C Levey, C Mcgray, I Paprotny, D Rus, An untethered, electrostatic, globally controllable mems micro-robot. *J. Microelectromechanical Syst.* **15**, 1–15 (2006).
22. (year?).
23. PRSaBS Vogtmann, D., A 25 mg magnetically actuated microrobot walking at 5 body lengths/sec. (2017).
24. K Islam, D Herman, A Leon, M Sarthak, Magnetosperm: A microrobot that navigates using weak magnetic fields. *Appl. Phys. Lett.* **104**, 223701–223701 (2014).
25. W Hu, GZ Lum, M Mastrangeli, M Sitti, Small-scale soft-bodied robot with multimodal locomotion. *Nature* **554**, 81–85 (2018).
26. K Ishiyama, M Sendoh, K Arai, Magnetic micromachines for medical applications. *J. Magn. Magn. Mater.* **242**, 41–46 (2002).
27. C Pawashe, S Floyd, M Sitti, Dynamic modeling of stick slip motion in an untethered magnetic microrobot. *Proc. Robotics: Sci. Syst. IV, Zurich, Switz.* (2008).
28. J Giltinan, P Katsamba, W Wang, E Lauga, M Sitti, Selectively controlled magnetic microrobots with opposing helices. *Appl. Phys. Lett.* **116** (2020).
29. HCESGSCDMSGQPTYHSPAMHDABJN Hongri Gu, Quentin Boehler, Magnetic cilia carpets with programmable metachronal waves. *Nat. Commun.* **11** (year?).
30. P Chytra, F Steven, S Metin, Multiple magnetic microrobot control using electrostatic anchoring. *Appl. Phys. Lett.* **94**, 164108–164108 (2009).

31. S Floyd, E Diller, C Pawashe, M Sitti, Control methodologies for a heterogeneous group of untethered magnetic micro-robots. *I. J. Robotic Res.* **30**, 1553–1565 (2011).
32. E Diller, M Sitti, Micro-scale mobile robotics. *Foundations Trends Robotics* **2**, 143–259 (2013).
33. S Floyd, C Pawashe, M Sitti, An untethered magnetically actuated micro-robot capable of motion on arbitrary surfaces in *2008 IEEE International Conference on Robotics and Automation*. pp. 419–424 (2008).
34. C Pawashe, S Floyd, M Sitti, Modeling and experimental characterization of an untethered magnetic micro-robot. *The Int. J. Robotics Res.* **28**, 1077–1094 (2009).
35. AW Mahoney, ND Nelson, KE Peyer, BJ Nelson, JJ Abbott, Behavior of rotating magnetic microrobots above the step-out frequency with application to control of multi-microrobot systems. *Appl. Phys. Lett.* **104**, 144101 (2014).
36. L Tianlong, et al., Janus microspheres: Janus microdimer surface walkers propelled by oscillating magnetic fields (adv. funct. mater. 25/2018). *Adv. Funct. Mater.* **28**, 1870173 (2018).
37. X Hui, et al., Reconfigurable magnetic microrobot swarm: Multimode transformation, locomotion, and manipulation. **4**, eaav8006 (2019).
38. Temel, Fatma, Y Serhat, Magnetically actuated micro swimming of bio-inspired robots in mini channels. pp. 342 – 347 (2011).
39. P Kathrin, Z Li, N Brad, Bio-inspired magnetic swimming microrobots for biomedical applications. *Nanoscale* **5** (2012).
40. H Choi, et al., Two-dimensional locomotion of a microrobot with a novel stationary electromagnetic actuation system. *Smart Mater. Struct.* **18**, 115017 (2009).
41. S Floyd, C Pawashe, M Sitti, An untethered magnetically actuated micro-robot capable of motion on arbitrary surfaces. *2008 IEEE Int. Conf. on Robotics Autom.* (2008).
42. C Yu, et al., Novel electromagnetic actuation system for three-dimensional locomotion and drilling of intravascular microrobot. *Sensors Actuators A: Phys.* **161**, 297–304 (2010).
43. L Zhang, et al., Artificial bacterial flagella: Fabrication and magnetic control. *Appl. Phys. Lett.* **94**, 064107 (2009).
44. K Vollmers, DR Frutiger, BE Kratochvil, BJ Nelson, Wireless resonant magnetic microactuator for untethered mobile microrobots. *Appl. Phys. Lett.* **92**, 144103 (2008).
45. T Xu, J Zhang, M Salehizadeh, O Onaizah, E Diller, Millimeter-scale flexible robots with programmable three-dimensional magnetization and motions. *Sci. Robotics* **4** (2019).
46. D Kim, T Wang, A Ansari, Magnetically-actuated micro-scale bristle-bots. (MARSS2020, IEEE Xplore), (2020) not published.
47. P Kumar, MG Krishna, AK Bhattacharya, Effect of microstructural evolution on magnetic properties of ni thin films. *Indian Acad. Sci.* (2009).
48. Ip-s (2016).
49. A Jake, E Olgac, K Michael, H Ann, N Brad, Modeling magnetic torque and force for controlled manipulation of soft-magnetic bodies. *IEEE Transactions on Robotics* **23**, 1247–1252 (2007).
50. U Parlak, ME Akpaz, ST Pzturk, M Erkovan, Thickness dependent magnetic properties of polycrystalline nickel thin films. *ACTA Phys. Polonica A* (2015).
51. Nanoscribe GmbH, *Photonic Professional GT*, (2013) Rev. 1.
52. HT L, Software techniques for two-and three-dimensional kinematic measurements of biological and biomimetic systems. *Bioinspiration & biomimetics* **3**, 034001 (2008).